

Nonlinear Observer Design for Visual-Inertial Odometry

Mouaad Boughellaba, Abdelhamid Tayebi, James R. Forbes, and Soulaimane Berkane

Abstract—This paper addresses the problem of Visual-Inertial Odometry (VIO) for rigid body systems evolving in three-dimensional space. We introduce a novel matrix Lie group structure, denoted $SE_{3+n}(3)$, that unifies the pose, gravity, linear velocity, and landmark positions within a consistent geometric framework tailored to the VIO problem. Building upon this formulation, we design an almost globally asymptotically stable nonlinear geometric observer that tightly integrates data from an Inertial Measurement Unit (IMU) and visual sensors. Unlike conventional Extended Kalman Filter (EKF)-based estimators that rely on local linearization and thus ensure only local convergence, the proposed observer achieves almost global stability through the decoupling of the rotational and translational dynamics. A globally exponentially stable Riccati-based translational observer along with an almost global input-to-state stable attitude observer are designed such that the overall cascaded observer enjoys almost global asymptotic stability. This cascaded architecture guarantees robust and consistent estimation of the extended state, including orientation, position, velocity, gravity, and landmark positions, up to the VIO unobservable directions (*i.e.*, a global translation and rotation about gravity). The effectiveness of the proposed scheme is demonstrated through numerical simulations as well as experimental validation on the *EuRoC MAV* dataset, highlighting its robustness and suitability for real-world VIO applications.

I. INTRODUCTION

Accurate estimation of vehicles' motion in GPS-denied environments is a fundamental problem in robotics. Among the available approaches, Visual-Inertial Odometry (VIO) has emerged as a promising solution by tightly fusing information from a camera and an inertial measurement unit (IMU). While VIO shares similarities with Simultaneous Localization and Mapping (SLAM), its primary objective is different: VIO focuses on estimating the ego-motion of the sensing platform without explicitly building or maintaining a persistent map of the surrounding environment. At the same time, VIO can be viewed as an extension of Visual Odometry (VO), where inertial data for the IMU are incorporated to improve the estimation accuracy with respect to the pure vision-based methods. This makes VIO a compelling choice

This work was supported by the National Sciences and Engineering Research Council of Canada (NSERC), under the grants NSERC-DG RGPIN 2020-06270 and NSERC-DG RGPIN-2020-04759, and by Fonds de recherche du Québec (FRQ).

M. Boughellaba and A. Tayebi are with the Department of Electrical Engineering, Lakehead University, Thunder Bay, ON P7B 5E1, Canada {mboughel, atayebi}@lakeheadu.ca.

S. Berkane is with the Department of Computer Science and Engineering, University of Quebec in Outaouais, Gatineau, QC, Canada. Soulaimane.Berkane@uqo.ca

J. R. Forbes is with the Department of Mechanical Engineering, McGill University, Montreal, QC, Canada. james.richard.forbes@mcgill.ca

for real-time applications. Cameras provide rich geometric information about the environment but suffer from scale ambiguity and sensitivity to illumination changes. Pure IMU-based odometry (relying on model integration) provides state estimates that drift over time due to sensors noise and biases. By combining these complementary sensing modalities, VIO achieves robust, accurate, and drift-resilient state estimation [1].

State-of-the-art solutions for VIO are predominantly based on two paradigms: filter-based approaches, typically using the extended Kalman filter (EKF), and optimization-based approaches, often realized through sliding-window optimization [2]. In EKF-based VIO, the system state is recursively propagated using IMU (gyro and accelerometer) measurements and corrected using visual observations. However, filter-based methods rely on local linearizations, which can lead to inconsistencies due to the accumulation of linearization errors. In contrast, optimization-based VIO formulates the motion estimation as a nonlinear least-squares problem, where recent poses and landmark positions are jointly optimized within a sliding time window. This category achieves higher accuracy, but it is computationally more demanding. As a result, the choice between EKF-based and optimization-based frameworks often reflects a trade-off between computational efficiency and estimation accuracy.

In this work, we propose a novel nonlinear geometric estimation framework for Visual-Inertial Odometry that realizes strong theoretical stability guarantees beyond those of existing approaches. Specifically, we formulate the VIO problem on a newly introduced matrix Lie group, denoted $SE_{3+n}(3)$, which provides a unified representation of the system's pose, velocity, gravity, and landmark positions within a consistent geometric structure. This formulation enables a design of an almost globally asymptotically stable observer that fuses IMU and visual measurements without relying on local linearization. The key idea is to exploit the natural geometry of the underlying state space to decouple the rotational and translational dynamics by introducing an auxiliary system related to the gravity vector. This leads to a cascaded observer structure. The translational subsystem is modeled as a linear time-varying system, for which a Riccati-based design ensures global exponential stability, while the rotational dynamics are governed by an almost globally input-to-state stable attitude observer. This design overcomes the limitations of conventional EKF- and optimization-based methods, which typically provide only local convergence guarantees or lack provable stability results. Through this development, we provide a rigorous geometric framework for VIO estimation that combines theoretical soundness with

practical robustness, and whose effectiveness is demonstrated through both numerical simulations and experimental validation on the *EuRoC MAV* dataset. The proposed observer estimates the system's extended state of the system, including orientation, position, velocity, gravity, and landmark positions up to the unobservable directions of VIO.

II. RELATED WORK

A. EKF- and optimization-based VIO

A landmark contribution in filter-based VIO was the Multi-State Constraint Kalman Filter (MSCKF) introduced by Mourikis et al. [3]. Unlike conventional EKF formulations that explicitly included 3D landmark positions in the state vector, the MSCKF introduced the idea of enforcing multi-view feature constraints without directly estimating landmark locations. This innovation drastically reduced the computational complexity from quadratic to linear in the number of visual features while maintaining estimator consistency, thereby enabling real-time operation on resource-constrained platforms. Following its introduction, several extensions of the MSCKF were proposed to enhance robustness and accuracy. For example, Mingyang *et al.* [4] demonstrated that the MSCKF algorithm achieves better accuracy and consistency than EKF-based VIO algorithms, due to its less restrictive probabilistic assumptions and delayed linearization, and further introduced the MSCKF 2.0 algorithm, which incorporates a closed-form expression for the IMU error-state transition matrix and fixed linearization states to ensure proper observability, while simultaneously performing online camera-to-IMU calibration. Beyond the classical MSCKF framework, further innovations focused on addressing the limitations of global reference frames and improving robustness in practical scenarios. Robocentric formulations were introduced to represent the state with respect to a moving local frame rather than a fixed global frame, improving numerical stability and estimator consistency during aggressive maneuvers [5], [6]. Around the same time, Bloesch et al. developed ROVIO [7], [8], an iterated EKF-based algorithm that departed from conventional feature-based approaches by employing a direct photometric error formulation, where image pixel intensities were integrated directly into the filter update. This approach reduced computational cost while maintaining robustness under challenging visual conditions. More recently, Geneva *et al.* introduced OpenVINS [9], a EKF-based framework that combines the MSCKF [3] with First-Estimates Jacobian (FEJ) treatments [10], [11] to achieve state-of-the-art performance. Its main contribution lies in offering a modular, open-source, and well-documented platform for EKF-based VIO research, providing a valuable baseline for comparing against optimization-based methods.

In addition to filtering-based approaches, optimization-based VIO methods have also emerged in the literature. A seminal contribution in this direction is OKVIS [12], which introduced a tightly coupled, keyframe-based estimator capable of supporting both monocular and stereo configurations. Building upon advances in visual SLAM, Qin *et al.* proposed VINS-Mono [13], which extended the

sliding-window formulation with efficient marginalization, loop closure, and global pose graph optimization, enabling drift reduction and high accuracy in large-scale environments. Complementing these developments, Delmerico and Scaramuzza [14] benchmarked a wide range of state-of-the-art VIO systems and showed that algorithms optimized primarily for speed and CPU efficiency often suffered from reduced accuracy and struggled on challenging datasets or resource-limited hardware.

B. Invariant and Equivariant Observers for VIO

Over the past decade, a growing body of work has investigated invariant and equivariant observers as alternatives to classical EKF- and optimization-based VIO, motivated by their ability to exploit Lie group symmetries to improve consistency and robustness. The two principal families are the Invariant EKF (IEKF) [15] and the more recent Equivariant Filter (EqF) [16]. Barrau and Bonnabel introduced the extended special Euclidean group $SE_2(3)$, which enables an exact linearization of IMU error dynamics when biases are known, thereby overcoming limitations of the standard on-manifold EKF and the multiplicative EKF widely used in SLAM and VIO. Subsequent studies analyzed observability properties of IEKF-based formulations [17] and compared their performance to conventional EKF-based approaches. Building on these foundations, Wu *et al.* [18] combined the MSCKF framework with invariant filtering principles to design a consistent Invariant MSCKF, addressing the growing inconsistency observed in the original MSCKF under Monte Carlo simulations. Extensions have also been made using unscented filters on Lie groups [19], as well as coupling IEKF with FEJ techniques to further enhance accuracy and consistency on real datasets such as TUM-VI [20].

Whereas the IEKF line of work has largely focused on refining error-state formulations within existing group structures, a complementary direction has emerged through the equivariant framework, which introduces novel Lie groups and filtering principles to systematically exploit measurement equivariance [16]. This approach aims to ensure that estimator outputs transform consistently under changes of the input reference frame. Recent advances have introduced novel Lie groups, such as $SE_n(m)$, which explicitly capture the symmetries inherent in SLAM and VIO problems [21]. Since the IEKF cannot always be directly applied to these higher-dimensional groups, the EqF framework provides a systematic approach to exploit measurement equivariance and mitigate linearization errors [16]. Building on this foundation, Van Goor *et al.* [22] extended these ideas to tightly coupled VIO, proposing a consistent equivariant filtering scheme that achieves lower linearization error in state propagation and employs higher-order equivariant output approximations than standard formulations. Their experimental evaluation on the EuRoC and UZH FPV datasets shows that the proposed method outperforms state-of-the-art VIO algorithms in both speed and accuracy. These results highlight that invariant and equivariant observers resolve theoretical consistency issues

and yield tangible performance gains in practice. This line of work positions geometric filtering as a powerful paradigm that complements EKF- and optimization-based frameworks, paving the way toward more reliable VIO in challenging real-world scenarios.

The remainder of this paper is structured as follows: Section III provides some preliminaries and the notations used in this paper, also, it introduces the new Lie matrix group $SE_{3+n}(3)$. Section IV defines the problem of visual-inertial odometry. Section V introduces the design of the proposed VIO observer with rigors observability analysis. Section VI reports simulation results, while Section VII presents experimental results based on the *EuRoC MAV* dataset. Finally, Section VIII concludes the paper.

III. PRELIMINARIES

A. Notations

The sets of real numbers and the n -dimensional Euclidean space are denoted by \mathbb{R} and \mathbb{R}^n , respectively. The set of unit vectors in \mathbb{R}^n is defined as $\mathbb{S}^{n-1} := \{x \in \mathbb{R}^n \mid x^\top x = 1\}$. Given two matrices $A, B \in \mathbb{R}^{m \times n}$, their Euclidean inner product is defined as $\langle\langle A, B \rangle\rangle = \text{tr}(A^\top B)$. The Euclidean norm of a vector $x \in \mathbb{R}^n$ is defined as $\|x\| = \sqrt{x^\top x}$, and the Frobenius norm of a matrix $A \in \mathbb{R}^{n \times n}$ is given by $\|A\|_F = \sqrt{\langle\langle A, A \rangle\rangle}$. The identity matrix is denoted by $I_n \in \mathbb{R}^{n \times n}$. The attitude of a rigid body is represented by a rotation matrix R which belongs to the special orthogonal group $SO(3) := \{R \in \mathbb{R}^{3 \times 3} \mid \det(R) = 1, R^\top R = I_3\}$. The tangent space of the compact manifold $SO(3)$ is given by $T_R SO(3) := \{R \Omega \mid \Omega \in \mathfrak{so}(3)\}$, where $\mathfrak{so}(3) := \{\Omega \in \mathbb{R}^{3 \times 3} \mid \Omega^\top = -\Omega\}$ is the Lie algebra of the matrix Lie group $SO(3)$. The map $[.]_\times : \mathbb{R}^3 \rightarrow \mathfrak{so}(3)$ is defined such that $[x]_\times y = x \times y$, for any $x, y \in \mathbb{R}^3$, where \times denotes the vector cross product on \mathbb{R}^3 . The angle-axis parameterization of $SO(3)$, is given by $\mathcal{R}(\theta, v) := I_3 + \sin \theta [v]^\times + (1 - \cos \theta) [v]^\times [v]^\times$, where $v \in \mathbb{S}^2$ and $\theta \in \mathbb{R}$ are the rotation axis and angle, respectively. The Kronecker product of two matrices A and B is denoted by $A \otimes B$. The *vectorization map* $(\cdot)^\vee : \mathbb{R}^{m \times n} \rightarrow \mathbb{R}^{mn}$ is defined by

$$([x_1 \ x_2 \ \dots \ x_n])^\vee = [x_1^\top, x_2^\top, \dots, x_n^\top]^\top, \quad (1)$$

where each $x_i \in \mathbb{R}^m$ for $i \in \{1, 2, \dots, n\}$. Notice that the map $(\cdot)^\vee$ stacks the columns of a matrix vertically into a single vector. The *inverse map*, denoted $(\cdot)^\wedge : \mathbb{R}^{mn} \rightarrow \mathbb{R}^{m \times n}$, is defined by

$$([x_1^\top, x_2^\top, \dots, x_n^\top]^\top)^\wedge = [x_1 \ x_2 \ \dots \ x_n], \quad (2)$$

which reconstructs the original matrix by reshaping the stacked vector back into its column-wise form. Let $\pi : \mathbb{R}^n \setminus \{0\} \rightarrow \mathbb{R}^{n \times n}$ denote the orthogonal projection operator, which will be used throughout this paper, defined by

$$\pi(x) = I_n - \frac{xx^\top}{\|x\|^2}, \quad (3)$$

where $x \in \mathbb{R}^n \setminus \{0\}$. The matrix $\pi(x)$ is an orthogonal projection that maps any nonzero vector in \mathbb{R}^n onto the

subspace orthogonal to x . It is bounded and positive semi-definite, satisfies $\pi(x)y = 0_{n \times 1}$ when x and y are collinear.

B. Matrix Lie Group for VIO

Inspired by [21], we propose a matrix Lie group structure specifically suited to the VIO problem. In particular, we define the matrix Lie group $SE_{3+n}(3) \subset \mathbb{R}^{(6+n) \times (6+n)}$ as follows:

$$SE_{3+n}(3) := \{X = \mathcal{M}(R, x_1, x_2, x_3, \mathbf{x}_L) :$$

$$R \in SO(3), x_1, x_2, x_3 \in \mathbb{R}^3, \mathbf{x}_L \in \mathbb{R}^{3 \times n}\}, \quad (4)$$

where the map $\mathcal{M} : SO(3) \times \mathbb{R}^3 \times \mathbb{R}^3 \times \mathbb{R}^3 \times \mathbb{R}^{3 \times n} \rightarrow \mathbb{R}^{(6+n) \times (6+n)}$ is defined as follows:

$$\mathcal{M}(R, x_1, x_2, x_3, \mathbf{x}_L) := \left[\begin{array}{c|cccc} R & x_1 & x_2 & x_3 & \mathbf{x}_L \\ \hline 0_{(3+n) \times 3} & & & & I_{3+n} \end{array} \right].$$

This construction generalizes the classical special Euclidean group $SE(3)$ by augmenting it with additional translational blocks corresponding to inertial states (e.g., velocity, gravity direction) and landmark positions. The block structure is carefully chosen such that group operations naturally encode both the rigid-body rotation and the translations associated with the inertial and landmark components. It is straightforward to verify that $SE_{3+n}(3)$ indeed forms a matrix Lie group. The group inverse is obtained as

$$X^{-1} = \mathcal{M}(R^\top, -R^\top x_1, -R^\top x_2, -R^\top x_3, -R^\top \mathbf{x}_L).$$

Furthermore, the group multiplication, defined as standard matrix multiplication, is closed, *i.e.*, for any $X_1, X_2 \in SE_{3+n}(3)$, the product $X_1 X_2$ is also an element of $SE_{3+n}(3)$. The identity element is simply the identity matrix I_{6+n} , *i.e.*, $X X^{-1} = X^{-1} X = I_{6+n}$, for every $X \in SE_{3+n}(3)$. The Lie algebra of the matrix Lie group $SE_{3+n}(3)$, denoted by $\mathfrak{se}_{3+n}(3) \in \mathbb{R}^{(6+n) \times (6+n)}$, is given as follows:

$$\mathfrak{se}_{3+n}(3) := \{V = \mathcal{V}(\Omega, x_1, x_2, x_3, \mathbf{x}_L) :$$

$$\Omega \in \mathfrak{so}(3), x_1, x_2, x_3 \in \mathbb{R}^3, \mathbf{x}_L \in \mathbb{R}^{3 \times n}\}, \quad (5)$$

where the map $\mathcal{V} : \mathfrak{so}(3) \times \mathbb{R}^3 \times \mathbb{R}^3 \times \mathbb{R}^3 \times \mathbb{R}^{3 \times n} \rightarrow \mathbb{R}^{(6+n) \times (6+n)}$ is defined as follows:

$$\mathcal{V}(\Omega, x_1, x_2, x_3, \mathbf{x}_L) := \left[\begin{array}{c|cccc} \Omega & x_1 & x_2 & x_3 & \mathbf{x}_L \\ \hline 0_{(3+n) \times 3} & & & & 0_{3+n} \end{array} \right].$$

Here, $\Omega \in \mathfrak{so}(3)$ denotes a skew-symmetric matrix encoding the infinitesimal rotation, while x_1, x_2, x_3 , and \mathbf{x}_L represent infinitesimal translations associated with the inertial and landmark states.

Remark 1: The matrix Lie group $SE_{3+n}(3)$ offers a compact and elegant representation that unifies rigid-body motions with additional translational states within a single algebraic framework. This formulation provides the foundation for developing our geometric observer for VIO in the subsequent sections.

C. Uniform Observability and Continuous Riccati Equation

Consider the following linear time-varying (LTV) system:

$$\dot{\mathbf{x}} = A(t)\mathbf{x} + B(t)\mathbf{u}, \quad (6)$$

$$\mathbf{y} = C(t)\mathbf{x}, \quad (7)$$

where $\mathbf{x}(t) \in \mathbb{R}^{n \times n}$, $\mathbf{u}(t) \in \mathbb{R}^\ell$, and $\mathbf{y}(t) \in \mathbb{R}^m$ denote the state, input, and output vectors of the system, respectively. The matrices $A(t)$, $B(t)$, and $C(t)$, with appropriate dimensions, are assumed to be continuous and bounded for all $t \geq 0$.

It is well known that the ability to reconstruct the system state from input–output data is closely related to the observability properties of the system. For time-invariant systems, the classical notion of observability, established via the rank condition of the observability matrix, provides a convenient test. In contrast, for time-varying systems, observability must be formulated in a uniform sense, requiring that sufficient excitation be maintained over finite time intervals. This requirement is formalized by the following definition [23].

Definition 1: The pair $(A(t), C(t))$ is said to be uniformly observable if there exist constants $\delta > 0$ and $\mu > 0$ such that $\forall t \geq 0$:

$$W(t, t+\delta) = \frac{1}{\delta} \int_t^{t+\delta} \Phi(\tau, t)^\top C(\tau)^\top C(\tau) \Phi(\tau, t) d\tau \geq \mu I_n, \quad (8)$$

where $\Phi(t, \tau)$ is the state transition matrix corresponding to $A(t)$, defined as the solution to $\frac{d}{dt}\Phi(\tau, t) = A(t)\Phi(\tau, t)$ with $\Phi(t, t) = I_n$. The matrix $W(t, t + \delta)$ is referred to as the *Observability Gramian (OG)* of the system (6)–(7). Note that the matrix $W(t, t + \delta)$ is naturally upper bounded by some constant since the matrices $A(t)$ and $C(t)$ are assumed to be bounded for all $t \geq 0$.

The observability property plays a fundamental role in the behavior of filtering and state estimation algorithms. In particular, it is directly connected to the solvability of the Continuous Riccati Equation (CRE), which arises as a key component in optimal filtering problems.

Definition 2: The *Continuous Riccati Equation (CRE)* is defined as

$$\begin{aligned} \dot{P}(t) &= A(t)P(t) + P(t)A(t)^\top \\ &\quad - P(t)C(t)^\top Q^{-1}(t)C(t)P(t) + V(t), \end{aligned} \quad (9)$$

where $P(0) \in \mathbb{R}^{n \times n}$ is a symmetric positive-definite matrix, and $V(t) \in \mathbb{R}^{n \times n}$, $Q(t) \in \mathbb{R}^{m \times m}$ are uniformly positive-definite and bounded matrices.

The following classical result establishes sufficient conditions for the global existence, uniqueness, and boundedness of the solution to (9).

Lemma 1 [24]: Suppose there exist constants $\delta > 0$, $\mu_v > 0$, and $\mu_q > 0$ such that for all $t \geq 0$:

$$\frac{1}{\delta} \int_t^{t+\delta} \Phi(t, \tau)^\top V(\tau)\Phi(t, \tau) d\tau \geq \mu_v I_n, \quad (10)$$

$$\frac{1}{\delta} \int_t^{t+\delta} \Phi(t, \tau)^\top C(\tau)^\top Q^{-1}(\tau)C(\tau)\Phi(t, \tau) d\tau \geq \mu_q I_n, \quad (11)$$

then the solution $P(t)$ of (9), for all $t \geq 0$, satisfies the uniform bounds

$$p_m I_n \leq P(t) \leq p_M I_n,$$

for some constants $0 < p_m \leq p_M < \infty$.

Remark 2: Conditions (10) and (11) are natural analogues of uniform controllability and uniform observability, respectively, and ensure that the solution $P(t)$ of (9) remains well conditioned. In particular, (10) and (11) are satisfied if $(A(t), C(t))$ is uniformly observable and $V(t)$ and $Q(t)$ are uniformly positive definite. These properties guarantee that the Riccati equation does not degenerate, thus preventing the solution $P(t)$ of (9) from either blowing up or collapsing to zero.

Remark 3: In the context of the Kalman filter, $V(t)$ and $Q(t)$ represent process and measurement noise covariances, respectively. Accordingly, Lemma 1 provides a rigorous justification for the stability of the Kalman filter under persistent excitation and uniform observability.

IV. PROBLEM STATEMENT

Let $\{\mathcal{I}\}$ and $\{\mathcal{B}\}$ be the inertial frame and the body-fixed frame attached to the center of mass of a rigid body, respectively. Consider the following dynamics of a rigid body and a set of n static landmarks:

$$\dot{R} = R[\omega^{\mathcal{B}}] \times \quad (12)$$

$$\dot{p} = v \quad (13)$$

$$\dot{v} = g + Ra^{\mathcal{B}} \quad (14)$$

$$\dot{p}_i = 0, \quad (15)$$

where $R \in SO(3)$ is the orientation of frame $\{\mathcal{B}\}$ with respect to frame $\{\mathcal{I}\}$, $p \in \mathbb{R}^3$ and $v \in \mathbb{R}^3$ denote the position and the linear velocity of the rigid body expressed in the inertial frame $\{\mathcal{I}\}$, $p_i \in \mathbb{R}^3$ is the position of the i -th landmark expressed in $\{\mathcal{I}\}$, $g \in \mathbb{R}^3$ is the acceleration due to gravity expressed in $\{\mathcal{I}\}$, $a^{\mathcal{B}} \in \mathbb{R}^3$ is the apparent acceleration capturing all non-gravitational forces applied to the rigid body expressed in $\{\mathcal{B}\}$, and $\omega^{\mathcal{B}}$ is the angular velocity of the rigid body expressed in $\{\mathcal{B}\}$. Figure 1 illustrates the VIO configuration for an example with four landmarks.

A. System representation on a matrix Lie group

The system dynamics (12)–(15) can be captured by a state evolving on the Lie group $SE_{2+n}(3)$ since the gravity vector g is constant and known. However, it is difficult to design an observer with global stability guarantees directly on this group due to the coupling resulting from the gravity direction when considering the group error. To remove this coupling, we extend the system with the additional (auxiliary) state g which satisfies:

$$\dot{g} = 0. \quad (16)$$

Although redundant from a physical standpoint, this auxiliary state eliminates the undesired coupling in the group error dynamics, thereby simplifying the observer design. The idea of introducing auxiliary states into the system to remove

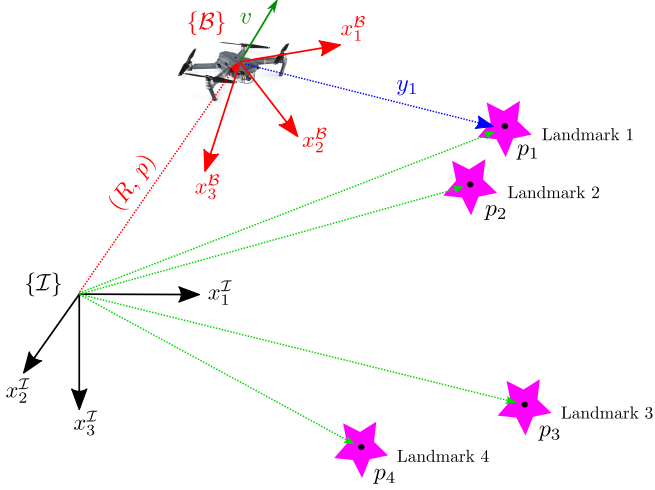


Fig. 1. Rigid body navigation in 3D with four unknown landmarks. The goal is to estimate the vehicle's extended pose (position, velocity, and orientation) based on landmark position estimates and available measurements.

coupling in the error dynamics has, for example, been used in [25] in the context of visual-inertial navigation with a known map. The resulting dynamics of (12)-(15) and (16) can be captured by considering the extended state $X = \mathcal{M}(R, p, v, g, \mathbf{p}_L)$, with $\mathbf{p}_L := [p_1 \ p_2 \ \dots \ p_n]$, which evolves on the higher-dimensional Lie group $SE_{3+n}(3)$. Consequently, the system dynamics can be written compactly as

$$\dot{X} = [X, H] + XV, \quad (17)$$

where the group velocity $V = \mathcal{V}([\omega^B]_\times, 0_{3 \times 1}, a^B, 0_{3 \times 1}, 0_{3 \times n})$ is derived directly from IMU measurements. The operator $[\cdot, \cdot]$ denotes the matrix Lie bracket, defined as $[X_1, X_2] = X_1 X_2 - X_2 X_1$ for any $X_1, X_2 \in \mathbb{R}^{(6+n) \times (6+n)}$. The constant matrix H is defined as

$$H = \left[\begin{array}{c|c} 0_3 & 0_{3 \times (3+n)} \\ \hline 0_{(3+n) \times 3} & S \end{array} \right]$$

$$\text{where } S = \begin{bmatrix} 0 & 0 & 0 & \dots & 0 & 0 \\ 1 & 0 & 0 & \dots & 0 & 0 \\ 0 & 1 & 0 & \dots & 0 & 0 \\ 0 & 0 & 0 & \dots & 0 & 0 \\ \vdots & \vdots & \vdots & \ddots & \vdots & \vdots \\ 0 & 0 & 0 & \dots & 0 & 0 \end{bmatrix} \in \mathbb{R}^{(3+n) \times (3+n)}.$$

Remark 4: In VIO, the IMU provides reliable short-term motion prediction, whereas visual measurements are essential for correcting accumulated drift. Within the group representation framework, this complementary relationship becomes explicit: the IMU determines the group velocity V , while visual observations constrain the system with respect to static landmarks.

B. Measurement models

In this section, we introduce the measurement models associated with the landmarks, which play a central role in VIO since the measurements obtained from

the camera determine the observable subspace of the system. Specifically, we consider three sensing modalities associated with the positions of the landmarks and the rigid body: relative position, relative stereo bearing, and relative monocular bearing. Each of these measurements is formulated using the matrix Lie group representation introduced in the previous section.

1) *Relative position measurements:* In this case, we assume that the relative position between the landmarks and the rigid body is measured in the body-fixed frame $\{\mathcal{B}\}$ and given as follows:

$$y_i = R^\top (p_i - p), \quad (18)$$

where $i \in \{1, 2, \dots, n\}$. Defining the vectors $\mathbf{y}_i := [(y_i)^\top \ r_i^\top]^\top \in \mathbb{R}^{6+n}$ and $\mathbf{r}_i := [0_{3 \times 1} \ r_i^\top]^\top \in \mathbb{R}^{6+n}$ where $r_i := [1 \ 0 \ 0 \ -e_i^\top]^\top \in \mathbb{R}^{3+n}$ with e_i denotes the i -th basis vector of \mathbb{R}^n , one can rewrite the measurements (18) as

$$\mathbf{y}_i = X^{-1} \mathbf{r}_i. \quad (19)$$

The measurement (18) corresponds to depth-capable sensors, such as RGB-D cameras, that directly provide relative position information. This type of measurement is particularly powerful because it removes the scale ambiguity inherent to bearing-only sensors. However, such measurements require active depth sensing hardware, which increases power consumption and is often limited to short ranges (e.g., indoor settings). From an observability perspective, direct position measurements offer stronger properties, as they reduce reliance on factors such as motion excitation to recover depth.

2) *Stereo-bearing measurements:* Let (R_{c1}, p_{c1}) and (R_{c2}, p_{c2}) denote the homogeneous transformations from the body frame $\{\mathcal{B}\}$ to the right and left camera frames, $\{\mathcal{C}_1\}$ and $\{\mathcal{C}_2\}$, respectively. The stereo-bearing vector measurement corresponding to the i -th landmark, expressed in the camera frame $\{\mathcal{C}_q\}$ with $q \in \{1, 2\}$, is modeled as

$$\bar{y}_i^q = \frac{R_{cs}^\top (R^\top (p_i - p) - p_{cq})}{\|R^\top (p_i - p) - p_{cq}\|}, \quad (20)$$

where $i \in \{1, 2, \dots, n\}$. Defining $\bar{\mathbf{y}}_i^q := [(\bar{y}_i^q)^\top \ 0_{1 \times (3+n)}]^\top \in \mathbb{R}^{6+n}$, one can verify that

$$\bar{y}_i^q = \frac{X_{cq}^{-1} (X^{-1} \mathbf{r}_i - \mathbf{p}_{cq})}{\|X_{cq}^{-1} (X^{-1} \mathbf{r}_i - \mathbf{p}_{cq})\|}, \quad (21)$$

where $X_{cq} := \mathcal{M}(R_{cq}, 0_{3 \times 1}, 0_{3 \times 1}, 0_{3 \times 1}, 0_{3 \times n})$ and $\mathbf{p}_{cq} := [p_{cq}^\top \ r_i^\top]^\top$ with $q \in \{1, 2\}$. Stereo-bearing measurements are widely used in VIO and SLAM due to their ability to recover depth through triangulation without requiring active depth sensors. Unlike relative position measurements, stereo-bearing measurements rely solely on passive cameras, which makes them well suited for outdoor and large-scale environments. Their accuracy, however, strongly depends on camera calibration, baseline length (i.e., the distance between the two camera centers that determines

the effective triangulation geometry), and the presence of sufficient visual texture for reliable correspondence matching. From an observability perspective, stereo systems provide depth information as long as the baseline is non-degenerate, positioning them as an intermediate modality between full relative position measurements and monocular-bearing observations.

3) Monocular-bearing measurements: Let (R_c, p_c) denote the homogeneous transformations from the body frame $\{\mathcal{B}\}$ to the camera frame $\{\mathcal{C}\}$. The monocular-bearing vector measurement corresponding to the i th landmark, expressed in the camera frame $\{\mathcal{C}\}$ is modeled as

$$\bar{y}_i = \frac{R_c^\top (R^\top (p_i - p) - p_c)}{\|R^\top (p_i - p) - p_c\|}, \quad (22)$$

where $i \in \{1, 2, \dots, n\}$. Defining $\bar{\mathbf{y}}_i := [(\bar{y}_i)^\top \ 0_{1 \times (3+n)}]^\top \in \mathbb{R}^{6+n}$, one has

$$\bar{\mathbf{y}}_i = \frac{X_c^{-1} (X^{-1} \mathbf{r}_i - \mathbf{p}_c)}{\|X_c^{-1} (X^{-1} \mathbf{r}_i - \mathbf{p}_c)\|}, \quad (23)$$

where $X_c := \mathcal{M}(R_c, 0_{3 \times 1}, 0_{3 \times 1}, 0_{3 \times 1}, 0_{3 \times n})$ and $\mathbf{p}_c := [p_c^\top \ r_i^\top]^\top$. Monocular-bearing measurements are the most common in vision-based navigation due to the ubiquity, low cost, and simplicity of single cameras. They are widely adopted in robotics and mobile devices since they require minimal hardware and can operate in a variety of environments. However, the key limitation of monocular sensing is the scale ambiguity: the absolute depth of landmarks cannot be inferred directly from a single image, which makes monocular systems dependent on additional information sources such as motion parallax. From an observability perspective, monocular bearings constrain only the direction of landmarks relative to the camera, while providing no direct constraint on the translation scale. This implies that the system is not fully observable without sufficient motion excitation. Thus, monocular-based VIO fundamentally relies on motion richness to achieve the desired performance. This is in contrast to stereo or depth sensors, which inherently resolve scale.

Remark 5: The bearing \bar{y}_i of the i -th landmark is obtained from its pixel coordinates (u_i, v_i) as

$$\bar{y}_i = \frac{\mathcal{K}^{-1} z_i}{\|\mathcal{K}^{-1} z_i\|} \in \mathbb{S}^2, \quad (24)$$

where $z_i = [u_i, v_i, 1]^\top$ and \mathcal{K} denotes the camera intrinsic matrix¹.

Remark 6: To ensure that the measurements in (20) and (22) are well defined for all time, we require that the camera center (given by the transformation (R_c, p_c) in the monocular case, and (R_{cq}, p_{cq}) with $q \in \{1, 2\}$ in the stereo case) does not coincide with any landmark point p_i . This assumption

¹The camera intrinsic matrix \mathcal{K} is a 3-by-3 calibration matrix that encodes the internal parameters of the camera, including focal lengths, skew, and the principal point. It maps 3D points in normalized camera coordinates to their corresponding pixel coordinates in the image plane.

guarantees that the denominator in (20) and (22) remains nonzero, thereby avoiding singularities in the measurement model. In practice, this assumption is naturally satisfied because cameras are rigid bodies with geometric dimensions rather than point masses.

Remark 7: Note that the three measurement types (18), (20), and (22) involve trade-offs between hardware complexity, computational cost, and observability: (i) relative position measurements (e.g., RGB-D) directly resolve depth and offer strong observability; (ii) stereo-bearing measurements balance hardware simplicity and depth inference; and (iii) monocular-bearing measurements are the most lightweight but introduce scale ambiguity. These distinctions highlight the importance of choosing the sensing modality according to the application requirements.

C. Objective

The objective is to design an observer that estimates the rigid body's extended states (orientation, position, velocity, and gravity) together with the landmark positions, based on the dynamics (17) and one of the measurement models (19), (21), or (23). This corresponds to a VIO problem, where the goal is to estimate the rigid body pose relative to the landmarks while simultaneously estimating the landmark positions. It is well established that VIO is subject to fundamental observability limitations: the global position cannot be recovered (only relative motion is observable), and the orientation about the gravity direction remains unobservable.

Remark 8: The observability limitations are not consequences of the proposed formulation, but inherent to VIO itself. Any consistent estimator must respect these structural constraints. Attempting to estimate unobservable quantities typically leads to inconsistency and divergence in practical implementations.

Remark 9: Unlike SLAM, the objective of VIO is not to reconstruct a global map, but rather to maintain a consistent trajectory estimate. In this formulation, landmarks primarily serve as temporary anchors that support inertial odometry and can be discarded or marginalized as the system evolves.

In the sequel, we propose an almost globally asymptotically stable observer that estimates the rigid body's extended states (orientation, position, velocity, and gravity) together with the landmark positions, up to an unknown constant translation and a rotation about the z -axis. This ensures that the proposed scheme remains consistent, as it preserves the fundamental observability properties of the VIO problem.

V. OBSERVER DESIGN

In view of (17), we propose the following VIO observer structure on $SE_{3+n}(3)$ with a copy of the dynamics plus an innovation term:

$$\dot{\hat{X}} = [\hat{X}, H] + \hat{X}V + \Delta\hat{X}, \quad (25)$$

where $\hat{X} = \mathcal{M}(\hat{R}, \hat{p}, \hat{v}, \hat{g}, \hat{\mathbf{p}}_{\mathbf{L}})$ is the estimated state, with $\hat{\mathbf{p}}_{\mathbf{L}} := [\hat{p}_1 \ \hat{p}_2 \dots \hat{p}_n]$, and $\Delta \in \mathfrak{se}_{3+n}(3)$ is an innovation term that will be designated later. Note that $\hat{R} \in SO(3)$,

$\hat{p} \in \mathbb{R}^3$, $\hat{v} \in \mathbb{R}^3$, $\hat{g} \in \mathbb{R}^3$ and $\hat{p}_i \in \mathbb{R}^3$ denote the estimates of R , p , v , g and p_i , for each $i \in \{1, 2, \dots, n\}$, respectively. Next, we derive the innovation term for each landmark measurement obtained from (19), (21), or (23). For each $i \in \{1, 2, \dots, n\}$, we define the following innovation term corresponding to the i -th landmark measurement:

$$\tilde{\mathbf{y}}_i = \begin{cases} \hat{X}^{-1} \mathbf{r}_i - \mathbf{y}_i, & \text{(relative-position),} \\ \sum_{q=1}^2 \pi(X_{cq} \bar{\mathbf{y}}_i^q) (\hat{X}^{-1} \mathbf{r}_i - \mathbf{p}_{cq}), & \text{(stereo bearing),} \\ \pi(X_c \bar{\mathbf{y}}_i) (\hat{X}^{-1} \mathbf{r}_i - \mathbf{p}_c), & \text{(monocular bearing).} \end{cases}$$

Moreover, by exploiting the properties of the projection map $\pi(\cdot)$, the innovation term associated with each landmark measurement can be written in the following form

$$\tilde{\mathbf{y}}_i = \Xi_i \left(\hat{X}^{-1} \mathbf{r}_i - X^{-1} \mathbf{r}_i \right), \quad (26)$$

where

$$\Xi_i = \begin{cases} I_{6+n}, & \text{(relative-position),} \\ \sum_{q=1}^2 \pi(X_{cq} \bar{\mathbf{y}}_i^q), & \text{(stereo bearing),} \\ \pi(X_c \bar{\mathbf{y}}_i), & \text{(monocular bearing).} \end{cases} \quad (27)$$

The projection map $\pi(\cdot)$, appearing in the definition of $\tilde{\mathbf{y}}_i$, is widely used for processing bearing measurements obtained from cameras [26], [25]. This projection is crucial because it preserves directional information while discarding unknown depth, allowing the observer to exploit geometric constraints for correction even when absolute distances are not available.

Let $Q := [I_3 \ 0_{3 \times (3+n)}]$. We introduce the following innovation term, constructed directly from the landmark-measurement innovation terms given in (26):

$$\sigma^p := (Q [\tilde{\mathbf{y}}_1, \tilde{\mathbf{y}}_2, \dots, \tilde{\mathbf{y}}_n])^\vee. \quad (28)$$

In pursuit of the previously defined objective, we propose the following innovation term to be incorporated into the VIO observer dynamics (25):

$$\Delta = \mathcal{V}(k_R [\sigma^R]_\times, \mathbf{K}_p(t) \sigma^p, \mathbf{K}_v(t) \sigma^p, \mathbf{K}_g(t) \sigma^p, (\Gamma(t) \sigma^p)^\wedge), \quad (29)$$

where $\sigma^R \in \mathbb{R}^3$, $k_R \in \mathbb{R}$, $\mathbf{K}_*(t) \in \mathbb{R}^{3 \times 3n}$, and $\Gamma(t) \in \mathbb{R}^{3n \times 3n}$. The proposed innovation term Δ consists of two main correction components: σ^R , which corrects the rotational motion (its expression will be designed later), and σ^p , which incorporates the landmark-based residuals required for translational correction. It is also important to note that, although Δ lies in $\mathfrak{se}_{3+n}(3)$, its construction deviates from gradient based approaches relying on potential functions typically used on matrix Lie groups. The key idea behind designing Δ using two separate correction terms, σ^R and σ^p , is to decouple the rotational motion from the translational motion, thereby allowing them to be treated as two cascaded subsystems. To see this, let us first derive the closed-loop system. Using the identity $\dot{\hat{X}}^{-1} = -\hat{X}^{-1} \dot{\hat{X}} \hat{X}^{-1}$ and

defining the right-invariant geometric error $E = X \hat{X}^{-1}$, it follows from (17) and (25) that

$$\dot{E} = [E, H] - E \Delta. \quad (30)$$

Here $E = \mathcal{M}(\tilde{R}, \tilde{p}, \tilde{v}, \tilde{g}, \tilde{\mathbf{p}}_L)$ where $\tilde{R} := R \hat{R}^T$, $\tilde{p} := p - \tilde{R} \hat{p}$, $\tilde{v} := v - \tilde{R} \hat{v}$, $\tilde{g} := g - \tilde{R} \hat{g}$ and $\tilde{\mathbf{p}}_L := [\tilde{p}_1 \ \tilde{p}_2 \ \dots \ \tilde{p}_n]$ with $\tilde{p}_i := p_i - \tilde{R} \hat{p}_i$. Now, let the error state of the translational subsystem be defined as

$$x = \left[(R^\top \tilde{v})^\top, (R^\top \tilde{g})^\top, ((R^\top (\mathbf{1} \otimes \tilde{p} - \tilde{\mathbf{p}}_L))^\vee)^\top \right]^\top. \quad (31)$$

The choice of the above translational error state x is motivated by the observability properties of the VIO system. The available measurements do not render absolute position or yaw observable. Instead, only body-frame velocity and gravity errors, together with relative landmark positions expressed in the body frame, can be reconstructed. Therefore, we define the translational error state using these observable combinations, which lie in the observable subspace of the VIO system and are invariant to the unobservable global position and yaw direction. Moreover, the correction term associated with the translational motion can be rewritten as

$$\sigma^p = \mathbf{C}(t) x, \quad (32)$$

where

$$\mathbf{C}(t) = \begin{bmatrix} 0_3 & 0_3 & \Pi_1 & 0_3 & \cdots & 0_3 \\ 0_3 & 0_3 & 0_3 & \Pi_2 & \cdots & 0_3 \\ \vdots & \vdots & \vdots & \vdots & \ddots & \vdots \\ 0_3 & 0_3 & 0_3 & 0_3 & \cdots & \Pi_n \end{bmatrix} \quad (33)$$

with $\Pi_i := Q \Xi_i Q^\top$ and Ξ defined in (27). Accordingly, we derive the following closed-loop dynamics for translational subsystem:

$$\dot{x} = (\mathbf{A}(t) - \mathbf{L}(t) \mathbf{C}(t)) x, \quad (34)$$

where

$$\mathbf{A}(t) = \begin{bmatrix} \mathbf{D}(t) & 0_{6 \times 3n} \\ B_n \otimes I_3 & I_n \otimes (-[\omega^B]_\times) \end{bmatrix} \quad (35)$$

$$\mathbf{L}(t) = (I_{n+2} \otimes \hat{R}^\top) \begin{bmatrix} \mathbf{K}_v(t) \\ \mathbf{K}_g(t) \\ \mathbf{1}^\top \otimes \mathbf{K}_p(t) - \Gamma(t) \end{bmatrix} \quad (36)$$

with

$$\mathbf{D}(t) = \begin{bmatrix} -[\omega^B]_\times & I_3 \\ 0_{3 \times 3} & -[\omega^B]_\times \end{bmatrix} \text{ and } B_n = [\mathbf{1}^\top \ 0_{n \times 1}]. \quad (37)$$

Furthermore, by designing $\sigma^R := \hat{g} \times g$, we derive the following dynamics for the rotational subsystem

$$\dot{\tilde{R}} = \tilde{R} \left[-k^R (\tilde{R}^\top g \times g) - \Upsilon(t) x \right]_\times, \quad (38)$$

where $\Upsilon(t) := [0_3 \ k^R g^\times \tilde{R}^\top \ 0_3 \ \dots \ 0_3] \in \mathbb{R}^{3 \times 3(n+2)}$. One checks that $\|\Upsilon(t)\|_F = \sqrt{2} k^R \|g\|$. Note that the innovation term for the rotational subsystem σ^R depends solely on a single vector, namely g and its estimate \hat{g} . As a result, the

attitude can only be estimated up to an arbitrary rotation about g [27]. To facilitate the stability analysis of (38), we therefore derive the following reduced attitude dynamics:

$$\dot{\check{g}} = k^R [\check{g} \times g]_{\times} \check{g} - [\check{g}]_{\times} \Upsilon(t) x, \quad (39)$$

where $\check{g} := \tilde{R}^T g$. The matrix $[\check{g}]_{\times} \Upsilon(t)$ is bounded since $\|\check{g}\| = \|g\|$ and $\|\Upsilon(t)\|_F = \sqrt{2}k^R\|g\|$. Now, let us establish the stability properties of the proposed VIO observer (25). Considering (34) and (39), one obtains the following overall closed-loop system:

$$\dot{\check{g}} = k^R [\check{g} \times g]_{\times} \check{g} - [\check{g}]_{\times} \Upsilon(t) x \quad (40)$$

$$\dot{x} = (\mathbf{A}(t) - \mathbf{L}(t)\mathbf{C}(t)) x. \quad (41)$$

The above closed-loop system can be seen as a cascaded nonlinear system evolving on $\mathbb{S}_g^2 \times \mathbb{R}^{3(n+2)}$ where $\mathbb{S}_g^2 := \{u \in \mathbb{R}^3 : u^T u = \|g\|^2\}$. Before establishing the stability properties of the closed-loop system (40)–(41), we first introduce an instrumental lemma that will be used in the subsequent stability analysis.

Lemma 2: Consider the matrix $\mathbf{A}(t)$ defined in (35) and the matrix $\mathbf{C}(t)$ defined in (33). The pair $(\mathbf{A}(t), \mathbf{C}(t))$ is uniformly observable if one of the following conditions holds:

- Relative-position measurements (18) or stereo-bearing measurements (20) are available, with at least one landmark being observed.
- Monocular-bearing measurements (22) are available, with at least one landmark being observed, and for each monocular-bearing measurement there exist constants $\delta^* > 0$ and $\mu^* > 0$ such that

$$\frac{1}{\delta^*} \int_t^{t+\delta^*} \pi(R(\tau) R_c y_i(\tau)) d\tau \geq \mu^* I_3, \quad (42)$$

for all $t \geq 0$.

Proof: See Appendix I ■

The relative-position-based design represents the most favorable scenario, as the measurements directly provide the relative positions of landmarks. In this case, the innovation term is linear in the error state, with $\mathbf{C}(t)$ being constant since $\Pi_i = I_3$ for each $i \in 1, 2, \dots, n$. Consequently, the system's observability is independent of the platform's motion. The stereo configuration lies between the relative position and monocular cases. While each camera individually provides bearing measurements without scale, the baseline between the two cameras introduces parallax², which allows depth to be inferred and resolves scale ambiguity. The time-varying nature of $\mathbf{C}(t)$ reflects the changing projections of landmarks in both cameras, though uniform observability is still achieved without requiring persistent platform excitation. From a practical standpoint, stereo cameras serve as a lightweight alternative to depth sensors, offering sufficient geometric constraints for state estimation, though they have higher hardware complexity than monocular setups.

²Parallax is the apparent displacement of an object viewed from two different positions, used in stereo vision to calculate depth by measuring the shift in position between corresponding points in two camera images.

Finally, the monocular case presents the greatest challenge, as bearing-only measurements cannot resolve depth. In this case, $\mathbf{C}(t)$ depends on the time-varying camera motion, and observability requires persistent excitation, as formalized by inequality (42). System motion, such as translation orthogonal to the line of sight, generates parallax, which helps disambiguate scale and ensures sufficient information for estimation. This highlights a key trade-off: while monocular setups are lightweight and cost-effective, their ability to guarantee consistent estimation heavily depends on the richness of the motion.

With Lemma 2 in place, we can now state the main result of this work.

Theorem 1: Assume that the matrices $Q(t)$ and $V(t)$ are strictly positive definite. Let $\mathbf{L}(t) = P(t)\mathbf{C}(t)^T Q^{-1}(t)$ where $P(t)$ is the solution of the CRE (9). Then, for any $k_R > 0$ and provided that the pair $(\mathbf{A}(t), \mathbf{C}(t))$ is uniformly observable, the equilibrium $(\check{g}, x) = (g, 0)$ of the system (40)–(41) is almost globally asymptotically stable³.

Proof: See Appendix II ■

The closed-loop system (40)–(41) consists of two cascaded subsystems: the first evolves on a reduced attitude dynamics manifold, \mathbb{S}_g^2 , a three-dimensional (scaled) sphere, while the second evolves in Euclidean space. Due to the topological obstruction of the 3-dimensional sphere [28], the almost globally asymptotically stable result in Theorem 1 represents the strongest stability achievable with continuous design. Furthermore, it is important to emphasize that the proposed design for the VIO observer (25) is deterministic in nature, and the theoretical results in Theorem 1 remain valid for any uniformly positive definite matrices Q and V . In other words, the convergence and stability guarantees do not rely on any probabilistic noise model.

Remark 10: The observer matrix gains $\mathbf{K}_p(t)$, $\mathbf{K}_v(t)$, $\mathbf{K}_g(t)$, and $\Gamma(t)$ are derived from the matrix $\mathbf{L}(t)$. Specifically, in view of (36), one has

$$\mathbf{K}_v(t) = [I_{3n} \ 0_{3n \times 3} \ 0_{3n \times 3}] \left(I_{n+2} \otimes \hat{R} \right) \mathbf{L}(t) \quad (43)$$

$$\mathbf{K}_g(t) = [0_{3n \times 3} \ I_{3n} \ 0_{3n \times 3}] \left(I_{n+2} \otimes \hat{R} \right) \mathbf{L}(t) \quad (44)$$

$$\mathbf{1}^T \otimes \mathbf{K}_p(t) - \Gamma(t) =$$

$$[0_{3n \times 3} \ 0_{3n \times 3} \ I_{3n}] \left(I_{n+2} \otimes \hat{R} \right) \mathbf{L}(t). \quad (45)$$

Note that the gains $\mathbf{K}_v(t)$ and $\mathbf{K}_g(t)$ are uniquely determined by the value of $(I_{n+2} \otimes \hat{R}) \mathbf{L}(t)$, whereas $\mathbf{K}_p(t)$ and $\Gamma(t)$ must be chosen to satisfy equation (45). Consequently, multiple valid choices exist for $\mathbf{K}_p(t)$ and $\Gamma(t)$. This non-uniqueness arises because the VIO system operates relative to the robot's own frame of reference (ego-centric). In essence, the selection of $\mathbf{K}_p(t)$ and $\Gamma(t)$ affects the estimated states but does not influence the closed-loop dynamics of the translational subsystem (34). A straightforward choice is to

³The equilibrium point is said to be almost globally asymptotically stable if it is stable, and attractive from all initial conditions except a set of zero Lebesgue measure.

set

$$\mathbf{K}_p(t) = 0_{3 \times 3n}$$

$$\boldsymbol{\Gamma}(t) = -[0_{3n \times 3} \ 0_{3n \times 3} \ I_{3n}] \left(I_{n+2} \otimes \hat{R} \right) \mathbf{L}(t).$$

Alternatively, one may exploit the static-environment property and determine the pair $(\mathbf{K}_p(t), \boldsymbol{\Gamma}(t))$ that minimizes an optimization criterion similar to that proposed in [29].

In contrast to state-of-the-art EKF-based VIO estimators, such as MSCKF [3], and more recent equivariant filters [22], which rely on local linearization and therefore guarantee only local convergence, the proposed VIO observer (25) achieves almost global asymptotic stability by decoupling the rotational and translational subsystems. Specifically, by introducing the additional (auxiliary) dynamics (16), the translational subsystem becomes a standalone linear time-varying system independent of attitude subsystem, for which a Riccati-based design yields a global exponentially stable translational observer. The rotational subsystem is treated separately, where we develop an almost globally input-to-state stable attitude observer. This cascaded structure enables the estimation of the rigid body's extended state (orientation, position, velocity, and gravity), together with landmark positions, up to the unobservable directions inherent to VIO (a global translation and a rotation about the z -axis), while ensuring almost global stability. The main trade-off of our approach lies in the use of constant, and hence non-optimal (in the Kalman filter sense), gain for the attitude observer (*i.e.*, the gain k_R), since the Riccati-based design applies only to the translational subsystem. Nonetheless, this trade-off is the cost of achieving a much stronger theoretical guarantee, providing stability results that go beyond the local convergence offered by EKF- and EqF-based VIO designs.

A. Implementation notes

To implement the proposed VIO observer (25), one may directly perform the state propagation on the tangent space of the matrix Lie group $SE_{3+n}(3)$, which offers improved computational efficiency. However, for practitioners with limited experience in matrix Lie groups, we provide below an explicit formulation of the proposed observer (25):

$$\dot{\hat{R}} = \hat{R}[\omega^B + \hat{R}^\top \sigma^R] \times \quad (46)$$

$$\dot{\hat{p}} = [\sigma^R] \times \hat{p} + \hat{v} + \hat{R} \sum_{j=1}^n K_j^p \sigma_j^p \quad (47)$$

$$\dot{\hat{v}} = [\sigma^R] \times \hat{v} + \hat{g} + \hat{R} a^B + \hat{R} \sum_{j=1}^n K_j^v \sigma_j^p \quad (48)$$

$$\dot{\hat{g}} = [\sigma^R] \times \hat{g} + \hat{R} \sum_{j=1}^n K_j^g \sigma_j^p \quad (49)$$

$$\dot{\hat{p}}_i = [\sigma^R] \times \hat{p}_i + \hat{R} \sum_{j=1}^n \Gamma_{ij} \sigma_j^p, \quad (50)$$

where $\sigma_j^p = Q \tilde{\mathbf{y}}_j$, $K_j^*(t)$ is the j -th 3×3 block of the matrix $\mathbf{K}_*(t)$, and $\Gamma_{ij}(t)$ is the (i, j) -th 3×3 block of the matrix $\boldsymbol{\Gamma}(t)$, for each $j \in \{1, 2, \dots, n\}$. Figure 2 illustrates the structure of the proposed nonlinear observer for VIO system.

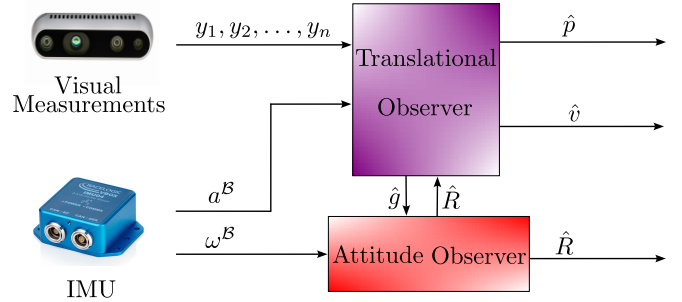


Fig. 2. Structure of the proposed VIO observer.

In practical applications, IMU measurements are typically available at a high rate, whereas vision-based measurements are obtained much less frequently due to sensor hardware limitations. Consequently, IMU data can be treated as continuous, while vision measurements are considered intermittent samples. Following the framework of Wang et al. [25], we redesign our continuous nonlinear VIO observer (46)–(50) to handle continuous IMU inputs and intermittently sampled vision measurements, as summarized in Algorithm 1.

Algorithm 1 Nonlinear observer for VIO

```

1: Input: Continuous IMU measurements, and intermittent
   visual measurements at times  $\{t_k\}_{k \in \mathbb{N}_{>0}}$ .
2: Output:  $\hat{R}(t), \hat{p}(t), \hat{v}(t), \hat{g}(t)$ , and  $\hat{p}_i(t)$  for all  $t \geq 0$ .
3: for  $k \geq 1$  do
4:   while  $t \in [t_{k-1}, t_k]$  do
5:      $\dot{\hat{R}} = \hat{R}[\omega^B + \hat{R}^\top \sigma^R] \times$ 
6:      $\dot{\hat{p}} = [\sigma^R] \times \hat{p} + \hat{v}$ 
7:      $\dot{\hat{v}} = [\sigma^R] \times \hat{v} + \hat{g} + \hat{R} a^B$ 
8:      $\dot{\hat{g}} = [\sigma^R] \times \hat{g}$ 
9:      $\dot{\hat{p}}_i = [\sigma^R] \times \hat{p}_i$ 
10:     $\mathbf{P} = \mathbf{A}(t)\mathbf{P} + \mathbf{P}\mathbf{A}^\top(t) + \mathbf{V}(t)$ 
11:   end while
12:   Obtain  $\sigma^p$  and  $\mathbf{C}(t)$  from visual measurements at  $t_k$ 
13:    $\mathbf{L} = \mathbf{P}\mathbf{C}^\top(t_k)(\mathbf{C}(t_k)\mathbf{P}\mathbf{C}^\top(t_k) + \mathbf{Q}(t_k))^{-1}$ 
14:   Compute  $\mathbf{K}_p, \mathbf{K}_v, \mathbf{K}_g, \boldsymbol{\Gamma}$  from  $\mathbf{L}$ 
15:    $\dot{\hat{R}}^+ = \hat{R}$ 
16:    $\dot{\hat{p}}^+ = \hat{p} + \hat{R} \sum_{j=1}^n K_j^p \sigma_j^p$ 
17:    $\dot{\hat{v}}^+ = \hat{v} + \hat{R} \sum_{j=1}^n K_j^v \sigma_j^p$ 
18:    $\dot{\hat{g}}^+ = \hat{g} + \hat{R} \sum_{j=1}^n K_j^g \sigma_j^p$ 
19:    $\dot{\hat{p}}_i^+ = \hat{p}_i + \hat{R} \sum_{j=1}^n \Gamma_{ij} \sigma_j^p$ 
20:    $\mathbf{P}^+ = (I_{3n+6} - \mathbf{L}\mathbf{C})\mathbf{P}$ 
21: end for

```

VI. SIMULATION

To evaluate the performance of the proposed scheme, we conducted a comprehensive simulation study using a rigid

body moving in three-dimensional space. The vehicle is equipped with an IMU and a camera system that provides measurements of the form (18), (20), and (22), which are referred to hereafter as *3D*, *SB*, and *MB*, respectively. The overall simulation setup is inspired by [30], but has been carefully extended with additional trajectory dynamics, noise models, and camera configurations in order to provide a more realistic setup.

Trajectory Generation: The simulated trajectory is designed to mimic a practical flight scenario for VIO. Specifically, the vehicle follows a circular path of radius 3 m in the horizontal plane, while simultaneously executing a vertical sinusoidal motion of amplitude 1.5 m and frequency 0.1 Hz. The forward linear velocity is fixed at 1 m/s, which results in a total path length of approximately 50 m. The total simulation time is therefore 50 s. In addition to the basic circular trajectory, we introduced small oscillations in roll (5° amplitude at 0.08 Hz) and pitch (3° amplitude at 0.06 Hz) to simulate natural attitude perturbations during flight. These oscillations prevent the motion from being overly idealized. The generated trajectory is depicted in Figure 3, where 1000 landmarks are randomly distributed on the walls of a cubic environment of side length 12 m. At each camera frame, a maximum of 50 visible landmarks are selected within a horizontal field of view (FOV) of 120°. This configuration ensures that the number of tracked features varies over time as in real-world scenarios.

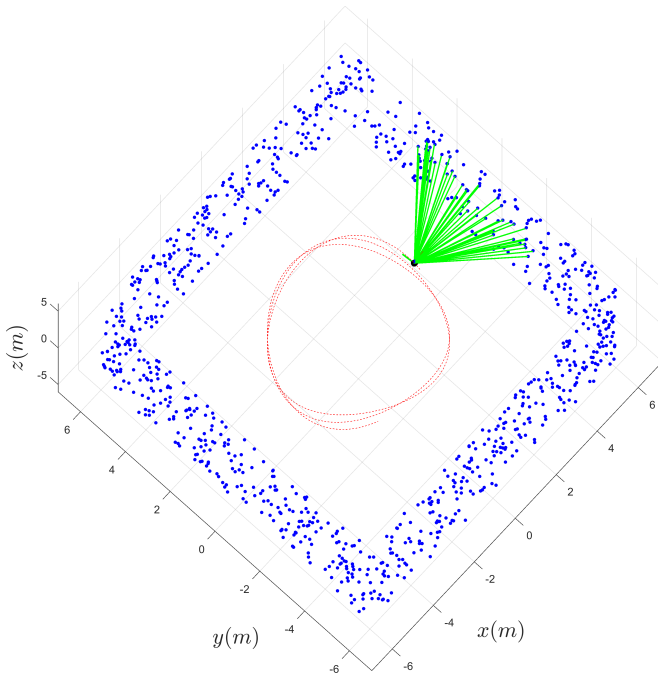


Fig. 3. The rigid body's true trajectory with circular-horizontal and sinusoidal-vertical motion, along with the randomly distributed landmarks on the surrounding walls. The animation video can be found at <https://youtu.be/yeboyXOtPiM>.

Sensor Characteristics and Noise Models: The IMU is sampled at 200 Hz, while the camera operates at 20 Hz. The IMU measurements are corrupted by additive Gaussian noise,

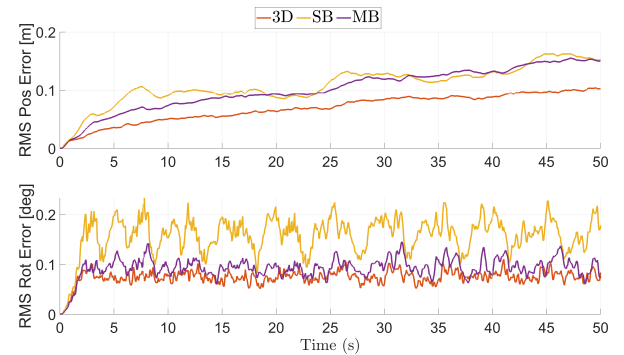


Fig. 4. Comparison of root-mean-squared errors averaged over 17 Monte Carlo simulations for the proposed VIO scheme across the three measurement models (18), (20), and (22).

with standard deviations of 0.0035 rad/s for the gyroscope and 0.095 m/s² for the accelerometer. For the camera, the bearing measurements (20) and (22) are corrupted by zero-mean Gaussian noise with a standard deviation of 0.5°, whereas the relative position measurement (18) is subject to a standard deviation of 0.05 m. This noise model captures the typical performance characteristics of low-cost IMU–camera systems. We also used the stereo extrinsics provided in the *EuRoC MAV* dataset [31].

Simulation Results and Discussion: To evaluate the performance of the proposed VIO scheme outlined in (46)–(50), we conduct a series of Monte Carlo simulations. The results of our proposed scheme, which incorporates 3D relative position measurements, are compared with those of an IEKF-based VIO framework that also utilizes 3D relative position measurements. The IEKF-based scheme, introduced in [32], was originally designed to address the SLAM problem, which shares the same objective of estimating the ego-motion of a rigid body. In this simulation, we disable the loop closure mechanism used in [32] and focus solely on the observer component to estimate ego-motion, extending it to incorporate the 3D relative position measurements defined in (18).

Figure 4 presents root-mean-squared errors averaged over 17 Monte Carlo simulations for the proposed VIO scheme across the three measurement models (18), (20), and (22). It clearly shows a drift over time, particularly in translational motion, which is expected since the proposed scheme preserves the fundamental observability properties of the VIO problem.

Figures 5 and 6 depict the time evolution of the rigid-body pose estimation errors, along with their 3σ uncertainty bounds, for both the IEKF-based scheme using 3D relative position measurements and the proposed VIO scheme under the three aforementioned measurement models. The results show that while the IEKF-based VIO scheme provides reasonable pose estimates, the proposed scheme achieves superior accuracy, as reflected by smaller uncertainties.

Figure 7 illustrates the estimated and true values of the body-frame gravity and linear velocity. The results clearly show that the proposed VIO scheme, under the measure-

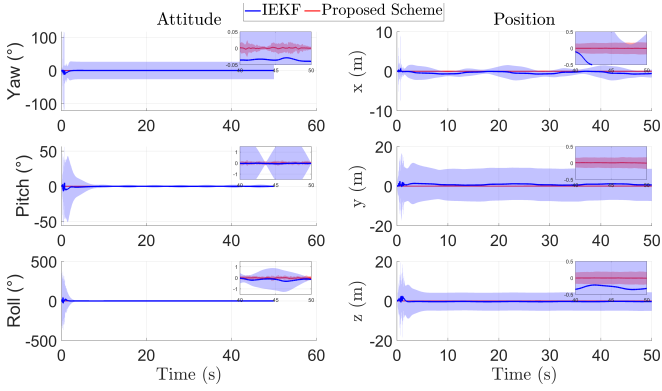


Fig. 5. Time evolution of the rigid-body pose errors with 3σ bounds, obtained using the IEKF-based and the proposed VIO schemes under the measurement model defined in (18). The results are based on Monte Carlo simulations with 17 runs.

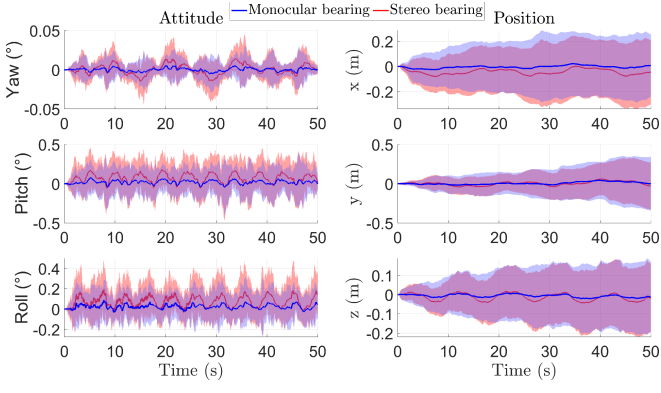


Fig. 6. Time evolution of the rigid-body pose errors with 3σ bounds, obtained using the proposed VIO schemes under the measurement model defined in (22) and (20). The results are based on Monte Carlo simulations with 17 runs.

ment models (18), (20), and (22), provides highly accurate estimates of both the gravity direction and the body-frame velocity throughout the trajectory, with no drift, as expected.

VII. EXPERIMENTAL RESULTS

To further validate the performance of the proposed VIO scheme under realistic sensing conditions, we evaluate it using real-world data from the *EuRoC MAV* dataset [31]. The *EuRoC MAV* dataset is a widely used benchmark for visual-inertial odometry, providing synchronized stereo camera images and IMU measurements recorded onboard a micro aerial vehicle operating in indoor environments, along with the ground truth.

Dataset Description and Experimental Setup: The *EuRoC MAV* dataset consists of multiple sequences recorded in machine hall (MH) and Vicon room (V) environments, featuring different levels of motion dynamics and visual complexity. In our experiments, we consider the sequences V1_01, V1_02, and V1_03.

The dataset provides stereo images at a rate of 20 Hz and IMU measurements at 200 Hz, which are directly compatible with the proposed observer structure. The stereo camera intrinsics and extrinsics, as well as the IMU-camera

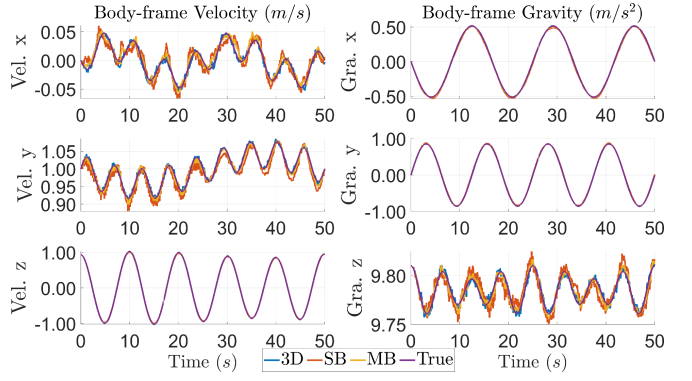


Fig. 7. Comparison of estimated and true values of body-fixed frame velocity and gravity under measurement models (18), (20), and (22). The results are based on Monte Carlo simulations with 17 runs.

calibration parameters, are taken directly from the dataset without modification. The ground-truth pose, obtained from a motion-capture system, is used solely for performance evaluation and is not employed by the estimator.

Feature detection and tracking are performed on stereo image pairs for measurements (18) and (20), and on the right camera images for measurement (22). At each camera frame, a varying number of visual features are tracked depending on the scene structure and motion, which naturally reflects realistic operating conditions. The proposed VIO scheme is implemented using the three measurement models defined in (18), (20), and (22).

Comparison Framework: The performance of the proposed approach is compared against an IEKF-based VIO framework adapted from [32]. For a fair comparison, similar to simulation setup, we disable the loop closure mechanism used in [32] and focus solely on the observer component to estimate ego-motion. Both methods are initialized using the same initial conditions and sensor calibration parameters.

Experimental Results and Discussion: Figures 8–10 illustrate the estimated body-frame velocity and body-frame gravity obtained with the proposed VIO scheme under the three considered measurement models, namely relative position, stereo bearing, and monocular bearing measurements. The results are shown for the V1_01, V1_02, and V1_03 sequences of the *EuRoC MAV* dataset and are compared against the corresponding ground-truth trajectories. Overall, the proposed observer exhibits stable and consistent convergence across all sequences and measurement configurations. In particular, the body-frame velocity and gravity estimates closely track the ground truth. These results corroborate the robustness of the proposed scheme, demonstrating its effectiveness under realistic sensing conditions. A more detailed comparison is presented in Table I, which reports the root-mean-square (RMS) position error for the IEKF-based VIO scheme using the relative position measurements (18), as well as for the proposed scheme under the measurement models (18), (20), and (22).

TABLE I
RMS RESULTS OF DIFFERENT SIMULATIONS FOR VARIOUS ROOMS.

Room Name	IEKF Scheme		Proposed Scheme	
	relative-positions	relative-positions	stereo bearings	monocular bearings
V1.01	0.63	0.70	0.77	0.81
V1.02	1.63	0.49	0.42	0.34
V1.03	1.96	1.78	0.33	0.39

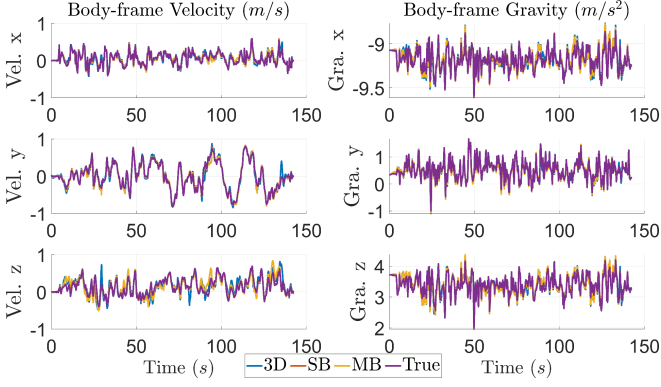


Fig. 8. Comparison of estimated and true values of body-frame velocity and gravity under measurement models (18), (20), and (22). The presented results correspond to the V1.01 sequence of the *EuRoC MAV* dataset.

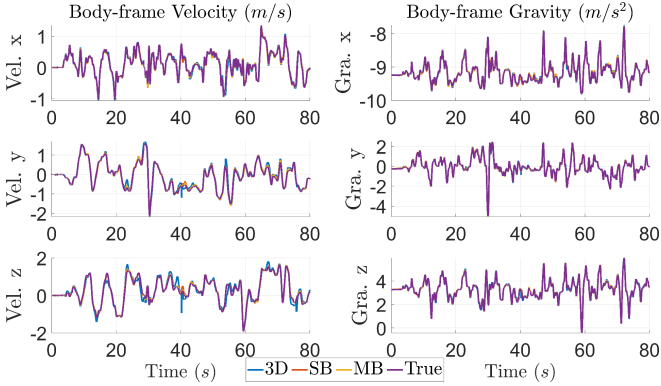


Fig. 9. Comparison of estimated and true values of body-frame velocity and gravity under measurement models (18), (20), and (22). The presented results correspond to the V1.02 sequence of the *EuRoC MAV* dataset.

VIII. CONCLUSIONS

This paper introduced a novel nonlinear geometric observer for visual-inertial odometry, formulated on the newly defined matrix Lie group $SE_{3+n}(3)$, which describes pose, gravity, linear velocity, and landmark positions within a consistent geometric framework. The proposed observer achieves almost global asymptotic stability for three distinct types of visual measurements: relative position, stereo bearing, and monocular bearing, demonstrating its generality and robustness. A key feature of the design lies in the use of a geometric error definition that naturally leads to a time-varying linear translational subsystem, thereby eliminating the need for local linearization. This property not only simplifies the observer design but also significantly enhances consistency compared to EKF-based and other linearization-dependent approaches. Moreover, by decoupling the rota-

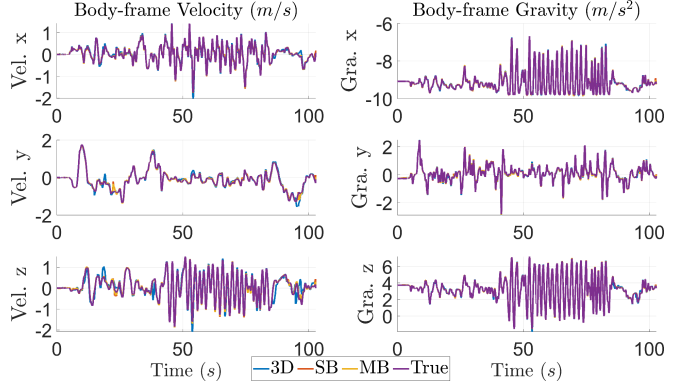


Fig. 10. Comparison of estimated and true values of body-frame velocity and gravity under measurement models (18), (20), and (22). The presented results correspond to the V1.03 sequence of the *EuRoC MAV* dataset.

tional and translational dynamics through the introduction of auxiliary dynamics, the observer adopts a cascaded structure in which the translational subsystem admits a Riccati-based (globally exponentially stable) estimator, while the rotational subsystem achieves almost global input-to-state stability. This structure guarantees consistent and robust estimation of the extended VIO state (*i.e.*, orientation, position, velocity, gravity, and landmark locations) up to the unobservable directions of global translation and rotation about gravity. The effectiveness of the proposed approach was validated through Monte Carlo simulations as well as experimental evaluations on the *EuRoC MAV* dataset, confirming its robustness under realistic sensing conditions. Future research will explore extensions of the proposed framework to account for IMU biases and to further assess its performance on additional real-world datasets. Additional efforts will also focus on deploying the proposed observer on embedded robotic platforms.

APPENDIX I PROOF OF LEMMA 2

The proof of this Lemma is motivated from [25]. Let $\mathbf{T}(t) = I_{n+2} \otimes R^\top(t)$, $\mathbf{S}(t) = I_{n+2} \otimes (-[\omega^B]_x)$ and $\bar{\mathbf{A}} = \mathbf{A}(t) - \mathbf{S}(t)$. Note that the matrix $\bar{\mathbf{A}}$ is a constant matrix and is given as $\bar{\mathbf{A}} = A \otimes I_3$, where A is defined as follows

$$A = \begin{bmatrix} D & 0_{2 \times n} \\ B_n & 0_{n \times n} \end{bmatrix}. \quad (51)$$

with $D = \begin{bmatrix} 0 & 1 \\ 0 & 0 \end{bmatrix}$ and B_n is given in (37). One can check that $\dot{\mathbf{T}}(t) = \mathbf{S}(t)\mathbf{T}(t)$ and $\mathbf{T}(t)\bar{\mathbf{A}} = \bar{\mathbf{A}}\mathbf{T}(t)$. Now, we will

demonstrate that the state transition matrix $\Phi(t, \tau)$ can be expressed as

$$\Phi(t, \tau) = \mathbf{T}(t) \bar{\Phi}(t, \tau) \mathbf{T}^{-1}(\tau), \quad (52)$$

where $\bar{\Phi}(t, \tau) = \exp(\bar{\mathbf{A}}(t - \tau))$ is the state transition matrix of $\bar{\mathbf{A}}$. Note that $\Phi(t, t) = I_n$, $\Phi^{-1}(t, \tau) = \Phi(\tau, t)$ and $\Phi(t_3, t_2)\Phi(t_2, t_1) = \Phi(t_3, t_1)$ for any $t_1, t_2, t_3 \geq 0$. To verify that $\Phi(t, \tau)$ is the state transition matrix associated with $\mathbf{A}(t)$, we will find its derivative with respect to t . It follows from (52) that

$$\frac{d}{dt} \Phi(t, \tau) = \dot{\mathbf{T}}(t) \bar{\Phi}(t, \tau) \mathbf{T}^{-1}(\tau) + \mathbf{T}(t) \frac{d}{dt} \bar{\Phi}(t, \tau) \mathbf{T}^{-1}(\tau).$$

Using the fact that $\frac{d}{dt} \bar{\Phi}(t, \tau) = \bar{\mathbf{A}} \bar{\Phi}(t, \tau)$, $\dot{\mathbf{T}}(t) = \mathbf{S}(t) \mathbf{T}(t)$ and $\mathbf{T}(t) \bar{\mathbf{A}} = \bar{\mathbf{A}} \mathbf{T}(t)$, one has

$$\frac{d}{dt} \Phi(t, \tau) = \mathbf{A} \Phi(t, \tau).$$

This implies that $\Phi(t, \tau)$ is the state transition matrix associated with $\mathbf{A}(t)$. Next, we establish the uniform observability of the pair $(\mathbf{A}(t), \mathbf{C}(t))$ by demonstrating the existence of constants $\delta > 0$ and $\mu > 0$ such that the observability Gramian satisfies the following condition

$$\mathbf{G}_\delta(t) = \frac{1}{\delta} \int_t^{t+\delta} \Phi(\tau, t)^\top \mathbf{C}(\tau)^\top \mathbf{C}(\tau) \Phi(\tau, t) d\tau \geq \mu I_{3n+6}. \quad (53)$$

To facilitate the analysis, the output matrix $\mathbf{C}(t)$ is expressed as

$$\mathbf{C}(t) = \mathbf{P}(t) \bar{\mathbf{C}},$$

where $\mathbf{P}(t) = \text{blkdiag}(\Pi_1, \dots, \Pi_n)$ and $\bar{\mathbf{C}} = [0_{3n \times 6} \quad I_{3n}]$. Invoking (52), together with the identities $\mathbf{T}^{-1}(\tau) = \mathbf{T}^\top(\tau)$ and

$$\bar{\mathbf{C}} \mathbf{T}(\tau) = (I_n \otimes R^\top(\tau)) \bar{\mathbf{C}},$$

the observability Gramian in (53) can be rewritten as

$$\begin{aligned} \mathbf{G}_\delta(t) &= \frac{1}{\delta} \int_t^{t+\delta} \Phi(\tau, t)^\top \mathbf{C}(\tau)^\top \mathbf{C}(\tau) \Phi(\tau, t) d\tau \\ &= \frac{1}{\delta} \mathbf{T}(t) \left(\int_t^{t+\delta} \bar{\Phi}(\tau, t)^\top \bar{\mathbf{C}}^\top \bar{\mathbf{P}}(\tau)^\top \bar{\mathbf{P}}(\tau) \bar{\mathbf{C}} \bar{\Phi}(\tau, t) d\tau \right) \mathbf{T}^{-1}(t), \end{aligned} \quad (54)$$

where $\bar{\mathbf{P}}(t) = (I_n \otimes R(t)) \mathbf{P}(t) (I_n \otimes R^\top(t))$. Note that $\bar{\mathbf{P}}(t) = \text{blkdiag}(\bar{\Pi}_1, \dots, \bar{\Pi}_n)$, where each $\bar{\Pi}_i$ is given by $\bar{\Pi}_i = R \Pi_i R^\top$ for $i = 1, 2, \dots, n$. To proceed with the proof, we analyze equation (54) separately for each measurement type, as carried out in the sequel.

Relative position measurements: Considering the landmark measurements provided in (19), one can verify that $\bar{\mathbf{P}}(t) = I_{3n}$, which further implies that

$$\mathbf{G}_\delta(t) = \frac{1}{\delta} \mathbf{T}(t) \left(\int_t^{t+\delta} \bar{\Phi}(\tau, t)^\top \bar{\mathbf{C}}^\top \bar{\mathbf{C}} \bar{\Phi}(\tau, t) d\tau \right) \mathbf{T}^{-1}(t). \quad (55)$$

Now, we are going to show that the pair $(\bar{\mathbf{A}}, \bar{\mathbf{C}})$ is (Kalman) observable. Let \mathcal{O} denote the observability matrix associated with the pair $(\bar{\mathbf{A}}, \bar{\mathbf{C}})$, which is given by

$$\mathcal{O} = \begin{bmatrix} I_n & 0_{n \times 2} \\ 0_n & B_n \\ 0_n & \bar{B}_n \\ 0_n & 0_{n \times 2} \\ \vdots & \vdots \\ 0_n & 0_{n \times 2} \end{bmatrix} \otimes I_3, \quad \text{where } \bar{B}_n = [0_{n \times 1} \quad \mathbf{1}^\top]. \quad (56)$$

Since $\det(\mathcal{O}^\top \mathcal{O}) \neq 0$, the observability matrix \mathcal{O} is full rank, which implies that the pair $(\bar{\mathbf{A}}, \bar{\mathbf{C}})$ is (Kalman) observable. Consequently, there exist positive constants $\bar{\delta} > 0$ and $\bar{\mu} > 0$ such that:

$$\frac{1}{\bar{\delta}} \int_t^{t+\bar{\delta}} \bar{\Phi}(\tau, t)^\top \bar{\mathbf{C}}^\top \bar{\mathbf{C}} \bar{\Phi}(\tau, t) d\tau \geq \bar{\mu} I_{3n+6}. \quad (57)$$

Substituting this back to (55) and choosing $\delta > \bar{\delta}$ and $0 < \mu \leq \frac{\bar{\delta} \bar{\mu}}{\delta}$, one concludes that

$$\mathbf{G}_\delta(t) \geq \mu I_{3n+6}, \quad (58)$$

for all $t \geq 0$. This implies that the pair $(\mathbf{A}(t), \mathbf{C}(t))$ satisfies the uniform observability condition under the measurement (19).

Stereo-bearing measurements: For the stereo-bearing measurements (21), one can show that Π_i is uniformly positive definite for each $i = 1, 2, \dots, n$, which also implies that $\bar{\mathbf{P}}(t)$ is uniformly positive definite, *i.e.*, $\bar{\mathbf{P}}(t) \geq \mu_{\bar{\mathbf{P}}} I_{3n}$ with $\mu_{\bar{\mathbf{P}}} > 0$. It follows from (54) that

$$\mathbf{G}_\delta(t) \geq \frac{\mu_{\bar{\mathbf{P}}}}{\delta} \mathbf{T}(t) \left(\int_t^{t+\delta} \bar{\Phi}(\tau, t)^\top \bar{\mathbf{C}}^\top \bar{\mathbf{P}}(\tau)^\top \bar{\mathbf{P}}(\tau) \bar{\mathbf{C}} \bar{\Phi}(\tau, t) d\tau \right) \mathbf{T}^{-1}(t). \quad (59)$$

Moreover, from (57) and (59), one can conclude that

$$\mathbf{G}_\delta(t) \geq \mu I_{3n+6}, \quad (60)$$

where $\delta > \bar{\delta}$ and $0 < \mu \leq \frac{\mu_{\bar{\mathbf{P}}} \bar{\delta} \bar{\mu}}{\delta}$. Inequality (60) confirms that the pair $(\mathbf{A}(t), \mathbf{C}(t))$ satisfies the uniform observability condition considering the stereo-bearing measurements (21).

Monocular-bearing measurements: Given the monocular-bearing measurements (23), where each measurement satisfies inequality (42) with constants $\delta^* > 0$ and $\mu^* > 0$, for $t \geq 0$, one can verify that

$$\frac{1}{\delta^*} \int_t^{t+\delta^*} \bar{\mathbf{P}}(\tau) d\tau > \mu^* I_{3n}, \quad (61)$$

for all $t \geq 0$. Consider inequality (61), along with the facts that $\bar{\mathbf{P}}^\top \bar{\mathbf{P}} = \bar{\mathbf{P}}$, the matrix $\bar{\mathbf{P}}$ is positive semi-definite, and the pair $(\bar{\mathbf{A}}, \bar{\mathbf{C}})$ is (Kalman) observable. According to [26, Lemma 2.7], it follows that there exist two constants $\bar{\delta} > 0$ and $\bar{\mu} > 0$ such that

$$\frac{1}{\bar{\delta}} \int_t^{t+\bar{\delta}} \bar{\Phi}(\tau, t)^\top \bar{\mathbf{C}}^\top \bar{\mathbf{P}}(\tau)^\top \bar{\mathbf{P}}(\tau) \bar{\mathbf{C}} \bar{\Phi}(\tau, t) d\tau \geq \bar{\mu} I_{3n+6}. \quad (62)$$

Furthermore, picking $\delta > 0$ and $\mu > 0$ such that $\delta > \bar{\delta}$ and $\mu \leq \frac{\bar{\mu} \bar{\delta}}{\delta}$, it follows from inequality (62) that

$$\mathbf{G}_\delta(t) \geq \mu I_{3n+6}, \quad (63)$$

This implies that the pair $(\mathbf{A}(t), \mathbf{C}(t))$ is uniformly observable under the monocular-bearing measurements (23). This completes the proof. \blacksquare

APPENDIX II PROOF OF THEOREM 1

Let us begin this proof by analyzing the stability properties of the translational subsystem (41). Consider the following real-valued function:

$$\mathcal{V}_P(x) = x^\top P^{-1} x, \quad (64)$$

where $P(t)$ is the solution of the CRE (9). Since the two matrices $Q(t)$ and $V(t)$ are uniformly positive definite, and the pair $(\mathbf{A}(t), \mathbf{C})$ is uniformly observable, it follows from Lemma 1 that $P(t)$, $\forall t \geq 0$, satisfies $p_m I_n \leq P(t) \leq p_M I_n$ for some constants $0 < p_m \leq p_M < \infty$. This implies that

$$\frac{1}{p_M} \|x\|^2 \leq \mathcal{V}_P(x) \leq \frac{1}{p_m} \|x\|^2. \quad (65)$$

Considering the dynamics (41), the time-derivative of \mathcal{V}_P is given by

$$\begin{aligned} \dot{\mathcal{V}}_P &= x^\top (P^{-1} \mathbf{A} + \mathbf{A}^\top P^{-1} - 2\mathbf{C}^\top Q\mathbf{C} + \dot{P})x \\ &= -x^\top P^{-1} V P^{-1} - x^\top \mathbf{C}^\top Q \mathbf{C} x \\ &\leq -\frac{v_m}{p_M^2} \|x\|^2 \leq -\rho \mathcal{V}_P, \end{aligned} \quad (66)$$

with $\rho = v_m \frac{p_m}{p_M^2}$ and $v_m = \inf_{t \geq 0} \lambda_{\min}^{V(t)}$ where $\lambda_{\min}^{V(t)}$ is the minimum eigenvalue of V at t . The last inequalities were derived using the facts $\dot{P}^{-1} = -P^{-1} \dot{P} P^{-1}$ and $\mathbf{C}^\top Q \mathbf{C} \geq 0$.

It follows from (66) that $\|x(t)\| \leq \sqrt{\frac{p_M}{p_m}} \exp\left(-\frac{\rho}{2}t\right) \|x(0)\|$, which implies that x converges to zero exponentially. Next, to establish the stability properties of the overall closed-loop system (40)-(41), we will first derive two results considering the reduced attitude closed-loop system (40). The first result establishes the stability properties of the system (40) with $x = 0$, and the second studies the Input to State Stability (ISS) properties of (40) with respect to x . Finally, we will conclude the stability properties of the overall system (40)-(41). The following lemma represents the first result related to the system (40) with $x = 0$.

Lemma 3: Let $k^R > 0$. Then, the following statements hold:

- System (40), with $x = 0$, has two equilibria: the desired equilibrium $\check{g} = g$ and the undesired one $\check{g} = -g$.
- The desired equilibrium $\check{g} = g$, for system (40) with $x = 0$, is almost globally asymptotically stable on \mathbb{S}_g^2 .

Proof: From (40), with $x = 0$, it is clear that the equilibrium points on \mathbb{S}_g^2 are $\check{g} = g$ and $\check{g} = -g$. The time-derivative of the following positive definite function $\mathcal{L}_1 = \frac{1}{2} \|g - \check{g}\|^2$, along the trajectories of (40) with $x = 0$, is given by $\dot{\mathcal{L}}_1 = -k^R \|g \times \check{g}\|^2$. The time-derivative of the following positive definite function $\mathcal{L}_2 = \frac{1}{2} \|g + \check{g}\|^2$,

along the trajectories of (40) with $x = 0$, is given by $\dot{\mathcal{L}}_2 = k^R \|g \times \check{g}\|^2$. Therefore, the equilibrium point $\check{g} = g$ is stable and the equilibrium point $\check{g} = -g$ is unstable (repeller). Almost global asymptotic stability on \mathbb{S}_g^2 of $\check{g} = g$ immediately follows. The time derivative of \mathcal{L}_1 and \mathcal{L}_2 were obtained using the fact that $u^\top [v]_x u = 0$ and $u^\top [u \times v]_x v = -\|u \times v\|^2$ for every $u, v \in \mathbb{R}^3$. This completes the proof of Lemma 3. \blacksquare

Next, we will study the ISS property of (40), with respect to x using the notion of almost global ISS introduced in [33].

Lemma 4: Given $k^R > 0$, the system (40) is almost globally ISS with respect to the equilibrium point $\check{g} = g$ and the input x .

Proof: From the fact that the system (41) is globally exponentially stable, it follows that the state x belongs to a compact set $\mathcal{A} \subset \mathbb{R}^{3(n+2)}$. This, together with the fact that \check{g} belongs to a compact manifold \mathbb{S}_g^2 , ensures that the system (40), subject to the bounded inputs x , evolves on the compact manifold $\mathbb{S}_g^2 \times \mathcal{A}$. Consequently, condition A0, given in [33], is fulfilled. Moreover, considering the positive definite function \mathcal{L}_1 and system (40) with $x = 0$, condition A1, given in [33], is also fulfilled. To check condition A2, given in [33], let us derive the first-order approximation of system (40) with $x = 0$. To do so, we apply small perturbation to \check{g} around the undesired equilibrium $-g$ through the attitude estimation error \tilde{R} by letting $\tilde{R} = \mathcal{R}_\alpha(\pi, \bar{u}) \exp([\zeta]_x)$, where $\bar{u} \perp g$ and $\zeta \in \mathbb{R}^3$ sufficiently small. Using the approximation $\exp([\zeta]_x) \approx I_3 + [\zeta]_x$ for sufficiently small ζ , we have $\check{g} = -g + [\zeta]_x g$. Letting $z := [\zeta]_x g$, one can see z as the small perturbation applied to \check{g} around the undesired equilibrium $-g$. By neglecting the cross terms and using the fact that $[u \times v]_x = vu^\top - uv^\top$ for every $u, v \in \mathbb{R}^3$, one has

$$\dot{z} = k^R M z, \quad (67)$$

where $M := \text{tr}(gg^\top)I_3 - gg^\top = \text{diag}(\|g\|^2, \|g\|^2, 0)$. This shows that the linearized dynamics of (40) with $x = 0$ have two identical positive eigenvalues $\|g\|$. Thus, condition A2 is also fulfilled. Now, consider the positive definite function \mathcal{L}_1 whose time derivative along the trajectories (40) is given by

$$\begin{aligned} \dot{\mathcal{L}}_1 &= -k^R \|g \times \check{g}\|^2 - g^\top [\check{g}]_x \Upsilon(t) x \\ &= -k^R \|g\| \|g - \bar{g}\|^2 - g^\top [\check{g}]_x \Upsilon(t) x \\ &= -k^R \|g\|^2 \|g - \bar{g}\|^2 - k^R \left(\|g\|^2 - 2\|g\|^2 g^\top \bar{g} \right. \\ &\quad \left. + (\bar{g}^\top g)^2 \right) - g^\top [\check{g}]_x \Upsilon(t) x. \end{aligned} \quad (68)$$

The last equality was obtained using the fact that $[u]_x^2 = -\|u\|^2 I_3 + uu^\top$ for every $u \in \mathbb{R}^3$. Next, let c_1 and c_2 be a constant scalars such that $-k^R(\|g\|^2 - 2\|g\|^2 g^\top \bar{g} + (\bar{g}^\top g)^2) \leq c_1$ and $\|g^\top [\check{g}]_x \Upsilon(t)\| \leq c_2$. One has

$$\dot{\mathcal{L}}_1 \leq -2k^R \|g\|^2 \mathcal{L}_1 + c_1 + c_2 \|x\|. \quad (69)$$

It follows from (69) that system (40) satisfies the ultimate boundedness property introduced in [33, Proposition 3].

Therefore, according to [33, Proposition 2], one can conclude that system (40) is almost globally ISS with respect to $\dot{g} = g$ and the input x . This completes the proof of Lemma 4. ■ Since the equilibrium $x = 0$ for the system (41) is UGES and the system (40) with $x = 0$ is AGAS and almost globally ISS with respect to x , one can conclude that the cascaded system (40)-(41) is AGAS. This completes the proof of Theorem.

REFERENCES

- [1] K. L. Lim and T. Bräunl, "A review of visual odometry methods and its applications for autonomous driving," *ArXiv*, vol. abs/2009.09193, 2020.
- [2] J. Gui, D. Gu, S. Wang, and H. Hu, "A review of visual inertial odometry from filtering and optimisation perspectives," *Advanced Robotics*, vol. 29, no. 20, pp. 1289–1301, 2015.
- [3] A. I. Mourikis and S. I. Roumeliotis, "A multi-state constraint kalman filter for vision-aided inertial navigation," in *Proceedings 2007 IEEE International Conference on Robotics and Automation*, 2007, pp. 3565–3572.
- [4] M. Li and A. I. Mourikis, "High-precision, consistent ekf-based visual-inertial odometry," *The International Journal of Robotics Research*, vol. 32, no. 6, pp. 690–711, 2013.
- [5] Z. Huai and G. Huang, "Robocentric visual-inertial odometry," *The International Journal of Robotics Research*, vol. 41, no. 7, pp. 667–689, 2022.
- [6] ———, "Robocentric visual-inertial odometry," in *2018 IEEE/RSJ International Conference on Intelligent Robots and Systems (IROS)*, 2018, pp. 6319–6326.
- [7] M. Bloesch, M. Burri, S. Omari, M. Hutter, and R. Siegwart, "Iterated extended kalman filter based visual-inertial odometry using direct photometric feedback," *The International Journal of Robotics Research*, vol. 36, no. 10, pp. 1053–1072, 2017.
- [8] M. Bloesch, S. Omari, M. Hutter, and R. Siegwart, "Robust visual inertial odometry using a direct ekf-based approach," in *2015 IEEE/RSJ International Conference on Intelligent Robots and Systems (IROS)*, 2015, pp. 298–304.
- [9] P. Geneva, K. Eckenhoff, W. Lee, Y. Yang, and G. Huang, "Openvins: A research platform for visual-inertial estimation," in *2020 IEEE International Conference on Robotics and Automation (ICRA)*, 2020, pp. 4666–4672.
- [10] G. P. Huang, A. I. Mourikis, and S. I. Roumeliotis, "Observability-based rules for designing consistent ekf slam estimators," *The International Journal of Robotics Research*, vol. 29, no. 5, pp. 502–528, 2010.
- [11] ———, "A first-estimates jacobian ekf for improving slam consistency," in *International Symposium on Experimental Robotics*, 2009.
- [12] S. Leutenegger, S. Lynen, M. Bosse, R. Siegwart, and P. Furgale, "Keyframe-based visual-inertial odometry using nonlinear optimization," *Int. J. Rob. Res.*, vol. 34, no. 3, p. 314–334, Mar. 2015.
- [13] T. Qin, P. Li, and S. Shen, "Vins-mono: A robust and versatile monocular visual-inertial state estimator," *IEEE Transactions on Robotics*, vol. 34, no. 4, pp. 1004–1020, 2018.
- [14] J. Delmerico and D. Scaramuzza, "A benchmark comparison of monocular visual-inertial odometry algorithms for flying robots," in *2018 IEEE International Conference on Robotics and Automation (ICRA)*, 2018, pp. 2502–2509.
- [15] A. Barrau and S. Bonnabel, "Invariant kalman filtering," *Annual Review of Control, Robotics, and Autonomous Systems*, vol. 1, no. 1, pp. 237–257, 2018.
- [16] P. van Goor, T. Hamel, and R. Mahony, "Equivariant filter (eqf)," *IEEE Transactions on Automatic Control*, vol. 68, no. 6, pp. 3501–3512, 2023.
- [17] T. Zhang, K. Wu, J. Song, S. Huang, and G. Dissanayake, "Convergence and consistency analysis for a 3-d invariant-ekf slam," *IEEE Robotics and Automation Letters*, vol. 2, no. 2, pp. 733–740, 2017.
- [18] K. Wu, T. Zhang, D. Su, S. Huang, and G. Dissanayake, "An invariant-ekf vins algorithm for improving consistency," in *2017 IEEE/RSJ International Conference on Intelligent Robots and Systems (IROS)*, 2017, pp. 1578–1585.
- [19] M. Brossard, S. Bonnabel, and A. Barrau, "Invariant kalman filtering for visual inertial slam," in *2018 21st International Conference on Information Fusion (FUSION)*, 2018, pp. 2021–2028.
- [20] Y. Yang, C. Chen, W. Lee, and G. Huang, "Decoupled right invariant error states for consistent visual-inertial navigation," *IEEE Robotics and Automation Letters*, vol. 7, no. 2, pp. 1627–1634, 2022.
- [21] A. Barrau and S. Bonnabel, "An ekf-slam algorithm with consistency properties," *arXiv:1510.06263*, 2016.
- [22] P. van Goor and R. Mahony, "Eqvio: An equivariant filter for visual-inertial odometry," *IEEE Transactions on Robotics*, vol. 39, no. 5, pp. 3567–3585, 2023.
- [23] C.-T. Chen, *Linear System Theory and Design*, 3rd ed. New York, NY: Oxford University Press, 1999.
- [24] R. Bucy, "Global theory of the riccati equation," *Journal of Computer and System Sciences*, vol. 1, no. 4, pp. 349–361, 1967.
- [25] M. Wang, S. Berkane, and A. Tayebi, "Nonlinear observers design for vision-aided inertial navigation systems," *IEEE Transactions on Automatic Control*, vol. 67, no. 4, pp. 1853–1868, 2022.
- [26] T. Hamel and C. Samson, "Position estimation from direction or range measurements," *Automatica*, vol. 82, pp. 137–144, 2017.
- [27] R. Mahony, T. Hamel, and J.-M. Pflimlin, "Nonlinear complementary filters on the special orthogonal group," *IEEE Transactions on Automatic Control*, vol. 53, no. 5, pp. 1203–1218, 2008.
- [28] J. Markdahl, J. Hoppe, L. Wang, and X. Hu, "A geodesic feedback law to decouple the full and reduced attitude," *Systems & Control Letters*, vol. 102, pp. 32–41, 2017.
- [29] P. van Goor, R. Mahony, T. Hamel, and J. Trumpf, "Constructive observer design for visual simultaneous localisation and mapping," *Automatica*, vol. 132, p. 109803, 2021.
- [30] C. Forster, L. Carbone, F. Dellaert, and D. Scaramuzza, "On-manifold preintegration for real-time visual-inertial odometry," *IEEE Transactions on Robotics*, vol. 33, no. 1, pp. 1–21, 2017.
- [31] M. Burri, J. Nikolic, P. Gohl, T. Schneider, J. Rehder, S. Omari, M. Achtelik, and R. Y. Siegwart, "The euroc micro aerial vehicle datasets," *The International Journal of Robotics Research*, vol. 35, pp. 1157 – 1163, 2016. [Online]. Available: <https://api.semanticscholar.org/CorpusID:9999787>
- [32] M. Brossard, A. Barrau, and S. Bonnabel, "Exploiting symmetries to design ekfs with consistency properties for navigation and slam," *IEEE Sensors Journal*, vol. 19, no. 4, pp. 1572–1579, 2019.
- [33] D. Angeli and L. Praly, "Stability robustness in the presence of exponentially unstable isolated equilibria," *IEEE Transactions on Automatic Control*, vol. 56, no. 7, pp. 1582–1592, 2011.